Deep Learning Strain Estimation: Is Physics-Based Simulation the Solution?

Thierry Judge, Nicolas Duchateau, Andreas Østvik, Khuram Faraz, Anders Austlid Taskén, Sigve Karlsen, Thor Edvardsen, Harald Brunvand, Md Abulkalam Azad, Havard Dalen, Bjørnar Grenne, Gabriel Kiss, Pierre-Yves Courand, Lasse Lovstakken, Pierre-Marc Jodoin, and Olivier Bernard

arXiv:2605.28697v1 [eess.IV] 27 May 2026

***Abstract*—Speckle tracking echocardiography (STE) is the clinical standard for myocardial strain estimation. Despite good performance on global strain (GLS), its accuracy for regional strain remains limited, even though this biomarker is highly relevant for early diagnosis and the characterization of subtle abnormalities. Deep learning is a promising alternative, but its development is constrained by the lack of reliable motion references. Existing solutions rely either on STE-derived labels or on simulations generated by physics-based models, but these synthetic sequences still have limited realism compared with clinical data. In this paper, we propose a novel simulation strategy that incorporates speckle decorrelation measures from real videos and uses an iterative refinement process to improve the motion realism in the simulations. We created an open-source photorealistic dataset of 1,478 videos with reference motion, which was used to train an echocardiographic motion estimation algorithm. The proposed method achieves unmatched performance on global and regional strain, notably reaching a GLS variability of 1.42% in an inter-expert setting compared to 1.78% for the clinical reference.** [1]

***Index Terms*—Deep learning, Echocardiography, Ultrasound simulation, Track any point (TAP), Myocardial strain**

T. Judge (thierry.judge@usherbrooke.ca) and P.-M. Jodoin, Dept. of Computer Science, University of Sherbrooke, Sherbrooke, Canada.

T. Judge, K. Faraz, N. Duchateau, P.-Y. Courand, and O. Bernard, INSA, Université Lyon 1, CNRS UMR 5220, Inserm U1206, CREATIS, Villeurbanne, France.

N. Duchateau and O. Bernard, Institut Universitaire de France (IUF).

P.-Y. Courand, Cardiology Dept., Hôpital Croix-Rousse, Hospices Civils de Lyon, Lyon, France, and the Cardiology Dept., Hôpital Lyon Sud, Hospices Civils de Lyon, Lyon, France.

A.-A. Taskén, and G. Kiss, Dept. of Computer Science, Faculty of Information Technology and Electrical Engineering, Norwegian University of Science and Technology (NTNU), Trondheim, Norway

A. Østvik, Md A. Azad, H. Dalen, B. Grenne, and L. Lovstakken, Dept. of Circulation and Medical Imaging, NTNU, Trondheim, Norway

S. Karlsen, and H. Brunvand, Department of Medicine, Hospital of Southern Norway, Arendal, Norway

A. Østvik, Md A. Azad, H. Dalen, and B. Grenne, Dept. of Cardiology and Cardiothoracic Surgery, St. Olavs Hospital, Trondheim, Norway

A. Østvik, Dept. of Health Research, SINTEF Digital, Trondheim, Norway

H. Dalen, Dept. of Medicine, Levanger Hospital, Nord-Trøndelag Hospital Trust, Levanger, Norway

T. Edvardsen, Dept. of Cardiology, Oslo University Hospital, Rikshospitalet and the Faaculty of Medicine, University of Oslo, Norway.

This work was supported in part by the NSERC's Discovery Grants and Canada Graduate Scholarships-Doctoral programs, the FRQNT Doctoral Training Scholarships, the French National Research Agency (LABEX PRIMES [ANR-11-LABX-0063] of Université de Lyon, and ORCHID [ANR-22-CE45-0029-01] projects) and by the Fédération Française de Cardiologie - FOCACHIA project 2025-2026.

[1]Code and database will be made public upon acceptance of this paper.

I. Introduction

Echocardiography is among the most widely recommended imaging modalities to quantify cardiac structure and function in routine clinical practice [1]. Segmentation of the cardiac chambers and myocardial wall enables the extraction of key volumetric and mass measurements. Tracking the myocardial wall across image sequences allows the estimation of local myocardial motion and myocardial deformation (also referred to as *strain*), a sensitive marker of early dysfunction [2]. Nonetheless, while segmentation has reached clinical expert-level performance through deep learning [3], myocardial tracking remains an open challenge even for the left ventricle (LV).

The current clinical standard, speckle tracking echocardiography (STE), relies on standard block matching and optical flow estimation without the use of deep learning. However, it assumes temporal coherence of speckle patterns [4], which is only valid over a limited number of consecutive frames within the cardiac cycle. In practice, this assumption is frequently violated due to speckle decorrelation induced by noise, imaging artifacts, fast cardiac motion, and out-of-plane motion. This leads to tracking errors that must be compensated for through extensive manufacturer-dependent tuning and regularization. As a result, myocardial strain estimation remains unreliable, particularly at the regional and local levels, despite its high relevance for assessing subtle disease patterns that are not accessible through global (i.e., myocardium-averaged) strain [5].

Deep learning offers a potential path to overcome these limitations. Two major strategies have been investigated in the literature so far: training motion estimation networks directly on STE-derived labels from real images [6], [7], or using simulated ultrasound data as ground truth [8], [9]. The first approach may inherit some of the biases of STE, which could limit its ability to outperform the method it aims to replace. The second approach is constrained by the realism of existing simulation pipelines, which assume temporally consistent speckle patterns and derive motion from simplified heart models [10] or 2D+t segmentations [8]. These simplifications lead to unrealistic textures and limited motion variability in the generated synthetic images, resulting in a substantial domain gap with respect to the targeted real clinical data.

In this work, we go one step further by developing a simulation pipeline to generate ultrasound videos with high spatial and temporal realism, specifically tailored for training deep learning–based methods. Our main contributions are:

- A consolidated simulation strategy that explicitly models

speckle decorrelation and generates synthetic ultrasound sequences closer to those from routine clinical imaging.
- An iterative dataset refinement strategy that leverages real patient data to progressively improve simulation realism and to generate a large-scale training dataset with physiologically plausible cardiac motion.
- A new motion estimation model *Track Any Speckle Network* in the myocardium (**TAS-Net**), based on CoTracker [11] and specifically tailored to the challenges of echocardiographic data, to enable the tracking of arbitrary speckle patterns.

Using 1,478 real echocardiographic videos spanning a wide range of textures and motion patterns, we generate a fully synthetic dataset with reference motion, which will be made openly available to support open and reproducible science. We demonstrate that this dataset enables the training of a high-performing motion estimation algorithm. Through extensive validation of both global and regional strain across multiple cohorts of real patients, we show that our method outperforms conventional STE and recent deep learning–based approaches, while avoiding their respective limitations. To the best of our knowledge, this work is the first to achieve such performance using exclusively simulated data, thereby enabling a new generation of deep learning–based methods for global and regional strain estimation in echocardiography.

II. Related Work

In recent years, deep learning has surpassed classical computer vision methods for optical flow estimation in natural videos. Key limitations, such as the scarcity of labeled training data, have been addressed through the use of large-scale synthetic datasets. Initial models such as PWC-Net [12] and RAFT [13] predicted dense optical flow between pairs of frames. Recently, research has shifted from dense frame-to-frame optical flow to sparse point-based tracking to better handle occlusions and long-range temporal dependencies, motivating the Track Any Point (TAP) task [14]. Being heavily driven by large-scale synthetic training datasets [15], [16], several models have been proposed [16]–[18].

Among recent advances, CoTracker stands out as one of the best-performing point-tracking models [11], [19]. It is a transformer-based architecture that performs joint tracking of multiple points. After extracting spatial features using a convolutional neural network, CoTracker encodes a token for each query point and applies cross-track and cross-time attention mechanisms to iteratively refine trajectory estimates, achieving state-of-the-art tracking accuracy.

In clinical practice, speckle tracking echocardiography primarily relies on block-matching algorithms to estimate apparent myocardial motion [20]. To mitigate limitations inherent to real echocardiographic image sequences, most notably speckle decorrelation, commercial tools rely on extensive manufacturer-specific tuning and regularization to produce smooth and physiologically plausible motion fields. This reliance constitutes a major limitation in terms of computational transparency and result reproducibility across vendors, an issue that has been a long-standing concern [21].

In recent years, deep learning has been increasingly adopted to provide data-driven solutions for myocardial motion estimation. As in natural image analysis, a major challenge in training deep learning models lies in the absence of reliable ground-truth motion. Several methods have explored learning from STE-derived labels. EchoTracker [6] employed a coarse-to-fine iterative tracking framework inspired by TAPIR [18] to estimate point trajectories along the myocardial centerline. Similarly, MyoTracker [7] proposed a simplified variant of CoTracker, removing the sliding window and iterative refinement mechanisms to enable fast and efficient tracking of right ventricular wall motion. While effective, such approaches can inherit the biases and limitations of STE-based supervision.

An alternative strategy relies on synthetic ultrasound data to provide motion ground truth. Evain *et al.* [8] proposed an adaptation of PWC-Net trained on 98 synthetic echocardiographic sequences derived from the CAMUS dataset and generated using the SIMUS simulator [22], demonstrating improved performance compared to block-matching–based baselines. More recently, Taskén *et al.* [9] compared RAFT and CoTracker for myocardial motion estimation in transesophageal echocardiography using a similar synthetic framework. Their results showed superior performance of CoTracker over RAFT.

Beyond network architectures, recent efforts have focused on improving the realism and scale of synthetic echocardiographic datasets. Among them, Burman *et al.* [10] introduced a large-scale dataset of 1,296 synthetic echocardiographic sequences generated from 50 patients from the CAMUS dataset using an advanced biophysical heart model (CircAdapt) [23] coupled with the COLE ultrasound simulator [24].

III. Method

Our work focuses on estimating LV myocardial motion from 2D echocardiographic image sequences, specifically apical 2-, 3-, and 4-chamber views. From the estimated motion, myocardial strain can then be derived with established clinical standards [25]. Our objective is to track a set of points representing myocardial motion throughout a video $\mathbf{V} \in [0,1]^{T\times H\times W}$, composed of T frames of height H and width W. To capture the full extent of myocardial motion while leveraging recent advances in joint point tracking, we represent the myocardium using a structured mesh $M \in \mathbb{R}^{l\times r\times 2}$, with l longitudinal and r radial points. This mesh is initialized at a given frame and subsequently propagated over time, yielding a spatio-temporal mesh $\mathbf{M} \in \mathbb{R}^{T\times l\times r\times 2}$.

To avoid the biases and limitations of STE-based methods, we propose in this section a new physics-based simulation pipeline specifically designed to generate synthetic echocardiogram videos with highly realistic temporal speckle patterns. It relies on a fully automated refinement strategy to generate large-scale synthetic datasets with efficient reference myocardial motion. Building on this unique synthetic dataset, we propose a point-tracking model adapted from the CoTracker architecture, with several critical modifications designed to achieve high performance on real echocardiographic sequences.

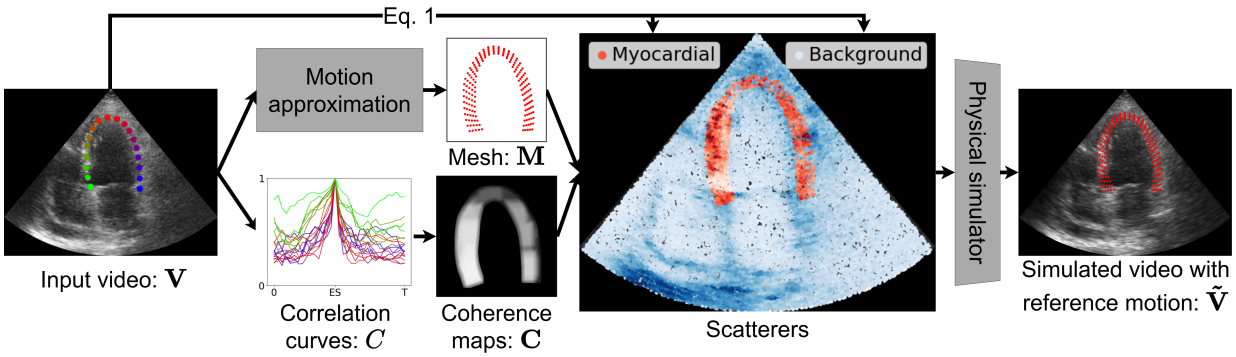

Fig. 1: Overview of the proposed simulation pipeline. Starting from an echocardiographic video and mesh approximating the myocardium motion, speckle correlation is estimated at each point (only a subset is depicted) to generate a dynamic coherence map. The resulting mesh and coherence maps control the generation of background and myocardial scatterers, which are used by the physical simulator to produce the synthetic images.

A. A new strategy for modeling speckle decorrelation

Our simulation pipeline relies on three complementary strategies designed to generate ultrasound textures with increasingly realistic time-varying speckle. First, we build upon a well-established simulation framework introduced in [8] (referred to as Strategy 1). We then incorporate explicit speckle decorrelation mechanisms to model controlled temporal variations of speckle patterns (Strategy 2). Finally, using an effective two-step refinement procedure, we further adjust the simulated time-varying speckle such that the resulting speckle decorrelation matches the one observed in a real echocardiographic sequence used as template (Strategy 3).

1) Strategy 1 (S1): Base simulation pipeline: As shown in Figure 1, our pipeline takes as input a real echocardiographic video $\mathbf{V}$, referred to as a template, and a temporal mesh $\mathbf{M}$ computed from the segmented myocardial region. This mesh provides a coarse approximation of the myocardial motion in the template, while its intrinsic regularization properties cause it to deviate from the true underlying motion.

At the core of the proposed workflow is the SIMUS physical simulator [22], specifically designed for ultrasound signal and image simulation. For each frame at time t of the simulated sequence, the simulator takes as input a collection of acoustic point scatterers indexed by i, characterized by their spatial coordinates (x_t^i, z_t^i) and their backscatter coefficients BSC_t^i. This coefficient is extracted from the corresponding real echocardiographic video according to:

$$\mathrm{BSC}_t^i = (\mathbf{V}_{t,x_t^i,z_t^i})^\gamma \cdot \epsilon, \qquad \epsilon \sim \mathcal{N}(0,1), \tag{1}$$

where γ is the gamma compression exponent and ϵ is a standard normal random variable.

As illustrated in Figure 1 and following [8], two categories of scatterers are considered: myocardial scatterers, which move according to the temporal mesh $\mathbf{M}$, and background scatterers, which populate the remainder of the image. To distinguish between these two populations, a static coherence map $\mathbf{C}^s \in [0,1]^{T\times H\times W}$ is constructed by weighting the myocardial masks with a probability parameter $p \in [0,1]$. To ensure a smooth transition between the myocardium and the background, the coherence value is linearly decreased from the myocardial boundary outward. Using the end-systolic (ES) frame as reference—chosen because the myocardium is largely visible within the imaging sector—scatterers are uniformly distributed across the ultrasound sector at a density of five per square wavelength. Myocardial scatterers are randomly sampled according to the coherence map evaluated at their spatial locations. Their backscatter coefficients remain fixed over time, while their positions evolve according to their relative coordinates within the temporal mesh. In contrast, background scatterers remain spatially fixed but their backscatter coefficients are updated at each frame according to Eq. (1). A subset of background scatterers, selected based on the coherence map, is also randomly introduced within the myocardium throughout the cardiac cycle to enhance speckle realism.

Given the combined set of myocardial and background scatterers at each frame, together with the probe configuration, SIMUS [22] generates synthetic raw radio-frequency (RF) echoes. These signals are subsequently demodulated to obtain the complex baseband signal, commonly referred to as the in-phase/quadrature (I/Q) signal. The I/Q signals are then beamformed using a conventional delay-and-sum approach to reconstruct B-mode images [26].

2) Strategy 2 (S2): Integrating speckle decorrelation: The simulation pipeline described above maintains a fixed ratio of coherent to incoherent scatterers, which in practice leads to overly coherent speckle patterns throughout the simulated sequence. To overcome this limitation, we introduce the approach illustrated in Figure 1, which adaptively updates the myocardial-to-background scatterer ratio based on information extracted from the real video. This process requires quantifying the speckle correlation present in the input data. To this end, the correlation between the end-systolic (ES) frame and all other time instants of the sequence is computed for each mesh point. A 25×25 window centered at the mesh point in the ES frame serves as a reference, and normalized two-dimensional correlation is computed with a window centered at the corresponding point location in each frame t. The maximum correlation value is retained to account for possible mesh misalignments, yielding a correlation array $C \in \mathbb{R}^{T\times l\times r}$.

These correlation curves are used to construct a dynamic

coherence map, $\mathbf{C}^d \in [0,1]^{T\times H\times W}$, obtained by bilinear interpolation over the myocardial mask, as illustrated in Figure 1. This map governs the relative amplitude contributions of myocardial and background scatterers. To avoid flickering artifacts caused by the temporal appearance or disappearance of scatterers, both populations are maintained concurrently within the myocardial region. Although this locally doubles the scatterer density, the total BSC amplitude is preserved. For each frame t, the BSC values of the myocardial m and background b scatterers are updated as:

$$\begin{cases} \mathrm{BSC}^i_{m,t} = \mathrm{BSC}^i_{m,ES} \cdot \mathbf{C}^d_{t,x^i_t,z^i_t}, \\ \mathrm{BSC}^i_{b,t} = \mathrm{BSC}^i_{b,t} \cdot \left(1 - \mathbf{C}^d_{t,x^i_t,z^i_t}\right). \end{cases} \tag{2}$$

This modulation of myocardial and background contributions induces time-varying speckle decorrelation that better matches real ultrasound behavior.

3) Strategy 3 (S3): Two-step refinement procedure: While the strategy described above improves the realism of the synthetic sequences, discrepancies in speckle decorrelation remain when compared with the original template sequences. To further align the simulated speckle decorrelation with that observed in the templates, we introduce a two-step refinement. First, a synthetic sequence is generated using Strategy 2, and the corresponding correlation curves, C_{sim}, are computed from the simulated output. The pointwise discrepancy between the target and simulated correlations is then defined as $C - C_{sim}$. A corrected set of input correlation curves is obtained according to $\tilde{C} = C + a \cdot (C - C_{sim})$, where the scaling factor a is empirically set to 2. Using these updated correlation curves, a new simulation is performed, resulting in speckle correlation dynamics that more closely match those observed in the template data.

B. A simulation strategy for enhanced reference motion

Despite the improved texture realism achieved by the previous strategies, the current simulation pipeline remains limited in terms of myocardial motion fidelity. This limitation stems from the reliance on 2D+t segmentation labels, which, through the adopted remeshing strategy, provide only a coarse approximation of true local myocardial motion. Alternative approaches have incorporated biomechanical heart models to derive more realistic motion patterns [27]. However, such methods typically rely on complex patient-specific personalization procedures, which substantially limit their scalability and practical deployment at scale. To mitigate these limitations, we introduce an innovative iterative simulation strategy inspired by the data engine of the Segment Anything Model (SAM) [28]. Following a similar philosophy, we develop a multi-stage refinement process.

Simulated dataset using temporal meshes from myocardial masks. Let $\mathcal{V} = \{\mathbf{V}_1, \mathbf{V}_2, ..., \mathbf{V}_N\}$ denote a set of N echocardiographic videos. Through either manual annotation or automated segmentation, a corresponding set of 2D+t segmentation masks is obtained, which can be converted into a collection of meshes approximating myocardial motion, denoted by $\mathcal{M}^0 = \{\mathbf{M}^0_1, ..., \mathbf{M}^0_N\}$. Given $\mathcal{V}$, $\mathcal{M}^0$, and the pipeline in fig. 1, an initial simulated dataset can be generated as $\mathcal{D}^0 = \{(\tilde{\mathbf{V}}^0_1, \mathbf{M}^0_1), ..., (\tilde{\mathbf{V}}^0_N, \mathbf{M}^0_N)\}$, where each $\tilde{\mathbf{V}}^0_i$ denotes a simulated video with the same dimensions as $\mathbf{V}_i$.

Simulated dataset using temporal meshes from a deep learning motion estimation model. Using the initial simulated dataset $\mathcal{D}^0$, an arbitrary deep learning motion estimation model is trained. This model is applied to the real video set $\mathcal{V}$ to predict refined, less regularized, and potentially more realistic temporal meshes. For each video $\mathbf{V}_i$, only a 2D segmentation is required to initialize the tracking process, resulting in an updated set of meshes $\mathcal{M}^1 = \{\mathbf{M}^1_1, ..., \mathbf{M}^1_N\}$. With $\mathcal{V}$ and $\mathcal{M}^1$, a new simulated dataset $\mathcal{D}^1 = \{(\tilde{\mathbf{V}}^1_1, \mathbf{M}^1_1), ..., (\tilde{\mathbf{V}}^1_N, \mathbf{M}^1_N)\}$ is generated. This refined dataset is subsequently used to train a new updated motion estimation model.

Multi-stage process. By combining an efficient segmentation model, such as [29], with the most recently trained motion estimation model, the previous step can be iteratively repeated in a fully automated manner to progressively increase both the realism and the size of the simulated dataset. For clarity, we keep N constant in the notation, although the number of videos in the dataset may vary across stages. Notably, in contrast to SAM, the predicted meshes are not manually validated at each iteration. Nevertheless, small motion estimation errors do not destabilize the proposed procedure, as the simulation step enforces exact motion in the generated images, consistent with the underlying meshes. This mechanism prevents the system from collapsing into a confirmation-bias loop, in which erroneous predictions would otherwise be progressively reinforced.

C. Track Any Speckle Network (TAS-Net)

The proposed synthetic dataset enables fully supervised training of deep learning models, thereby facilitating their adaptation to the temporal characteristics of echocardiographic image sequences. Among existing approaches, EchoTracker [6] represents a strong baseline; however, recent advances in joint point tracking suggest that improved performance may be achievable for this task. In particular, CoTracker-based models benefit from jointly tracking multiple points, which is especially advantageous in regions with low temporal correlation. Within this family of methods, MyoTracker [7] has recently been proposed as a low-latency alternative, achieving performance close to that of CoTracker while prioritizing computational efficiency. In contrast, our work adopts the opposite design choice, prioritizing high tracking accuracy while maintaining a reasonable processing time on the order of a few seconds, consistent with clinical practice. To this end, we design a set of targeted adaptations to the CoTracker architecture, yielding an efficient model for echocardiographic video analysis. By preserving the core architecture, the proposed approach benefits from pretrained weights learned on large-scale natural video datasets, a key factor for stability and performance in our iterative training process when simulated data are scarce.

1) A mesh embedding for improved spatio-temporal coherence: In CoTracker's default configuration, the transformer input token associated with a point k at time t is constructed by

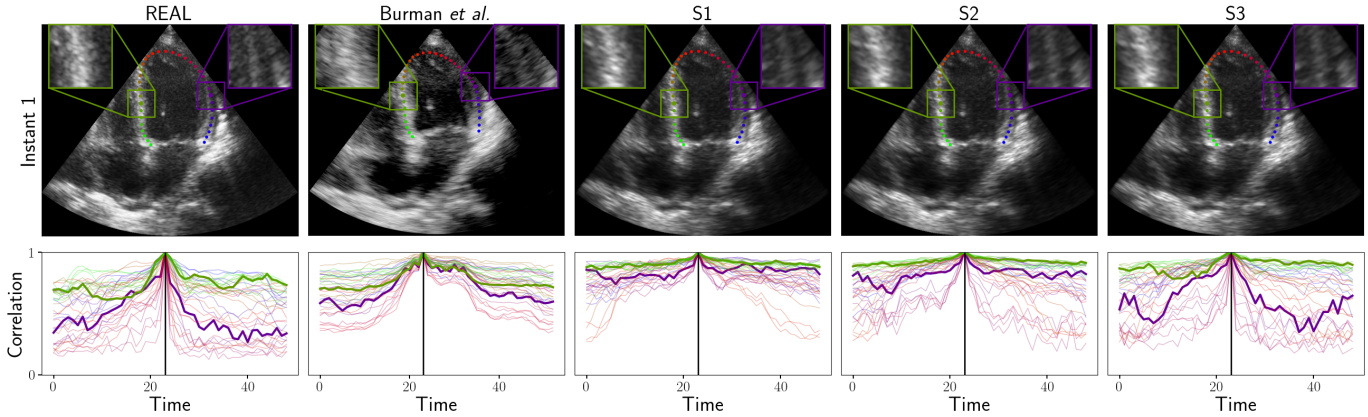

Fig. 2: Sample frames from a simulated sequence and its corresponding real template sequence are shown. The last row displays correlation curves computed for the 36 centerline points, with highlighted curves corresponding to points located within the zoomed image regions. Note that the simulation proposed by Burman *et al.* has a different sequence length.

concatenating position ($\hat{P}_t^k$), visibility ($\hat{v}_t^k$), appearance (Q_t^k), correlation (C_t^k), and positional encoding (η and η') features, and is defined as:

$$G_t^k = \Big(\hat{P}_t^k - \hat{P}_1^k; \hat{v}_t^k; Q_t^k; C_t^k; \eta(\hat{P}_t^k - \hat{P}_1^k) + \eta'(\hat{P}_1^k) + \eta'(t)\Big).$$

In the default configuration, each transformer token G_t^k does not encode any explicit information linking it to a specific mesh point. To address this limitation, we introduce a mesh-position embedding that is added to the appearance vector Q_t^k. Specifically, a time-invariant embedding E^k is defined for each mesh point k as $E^k = \psi(l_k, r_k)$ where l_k and r_k denote the normalized longitudinal and radial coordinates of the mesh point, respectively, with values in $[0, 1]$. The function ψ is implemented as a multilayer perceptron with three hidden layers (32, 64, and 128 neurons), with the output dimensionality matching that of the appearance vector Q. At each iteration, the mesh-aware appearance vector is defined as $\bar{Q}_t^k = Q_t^k + E^k$, and is used in the construction of the transformer input tokens. By relying on a continuous embedding conditioned on normalized mesh coordinates, the proposed formulation enables the model to be trained and applied to meshes with varying spatial resolutions and different numbers of mesh points.

2) A continuous visibility score for explicit modeling of speckle decorrelation: The default CoTracker model outputs not only point trajectories but also a binary visibility indicator for each point at each time frame to handle occlusions. We leverage this mechanism to explicitly incorporate speckle decorrelation into our model. Specifically, the binary visibility indicator is extended to a continuous visibility score, enabling the prediction of the degree of speckle decorrelation at each point. When trained on the proposed simulations with varying correlation levels, the network learns to regress the speckle correlation value using a mean squared error loss.

3) A bidirectional sliding-window strategy for training and inference: In CoTracker, points can be initialized at any time within a video and subsequently tracked across the remaining frames. However, since the myocardium is typically more visible within the ultrasound sector at the end-systolic (ES) frame we initialize all mesh points at ES. In contrast to recent studies [9], we adopt a bidirectional tracking strategy during both training and inference. Specifically, we replace CoTracker V1's forward-only sliding-window scheme with a bidirectional sliding-window formulation. The model is initialized at the ES frame and predicts point trajectories forward from ES to the end of the sequence, as well as backward from ES to the beginning. We retain the original window overlap strategy, whereby consecutive windows overlap by half of their extent, and predictions in the overlapping region are used to initialize or constrain the subsequent window to ensure temporal consistency.

During training, CoTracker operates on temporal crops extracted from the full sequence. In the default configuration, crops are sampled randomly and initialization occurs at the first frame of each crop. However, as our correlation-based prediction requires access to the ES frame to estimate relative visibility, we modify the sampling strategy to enforce that each training crop includes the ES frame. A direct consequence of always initializing at ES is a reduction in the diversity of crop–query configurations observed during training: with ES-fixed initialization, each video effectively contributes a single initialization condition, rather than multiple conditions across different crops. To preserve this diversity and improve generalization, we therefore initialize the model at an arbitrary frame during training—while still ensuring that the crop contains the ES frame. At inference, initialization is performed exclusively at ES, in accordance with the intended clinical workflow.

IV. Experimental setup

A. Datasets used in this study

1) Training: Data used in our simulation pipeline were obtained from the CAMUS and CARDINAL datasets. CAMUS [30] comprises apical two-chamber (A2C) and four-chamber (A4C) views from 500 patients. Manual annotations of the LV endocardium and epicardium, as well as the left atrium, were performed by a senior cardiologist for both end-diastolic (ED) and end-systolic (ES) frames. In addition, a subset of 98 4CH videos was manually annotated over

TABLE I: Mean trajectory error (MTE, in mm) computed for the different configurations of the proposed multi-stage strategy. Best values are in **bold**.

Version	Strategy	Size	SSHF (↓)	HUNT(↓)
$\mathcal{D}^0$	S1	242	$1.21_{\pm 0.02}$	$1.42_{\pm 0.01}$
$\mathcal{D}^0$	S2		$1.21_{\pm 0.04}$	$1.50_{\pm 0.04}$
$\mathcal{D}^1$	S1 → S1	1,478	$1.20_{\pm 0.02}$	$1.33_{\pm 0.02}$
$\mathcal{D}^1$	S2 → S2		$\mathbf{1.15}_{\pm \mathbf{0.01}}$	$1.37_{\pm 0.02}$
$\mathcal{D}^1$	S1 → S2		$1.16_{\pm 0.01}$	$1.31_{\pm 0.02}$
$\mathcal{D}^2$	S1 → S1 → S1	1,478	$\mathbf{1.15}_{\pm \mathbf{0.00}}$	$1.33_{\pm 0.01}$
$\mathcal{D}^2$	S2 → S2 → S2		$\mathbf{1.15}_{\pm \mathbf{0.00}}$	$1.34_{\pm 0.02}$
$\mathcal{D}^2$	S1 → S2 → S2		$1.16_{\pm 0.00}$	$1.32_{\pm 0.01}$
$\mathcal{D}^2$	S1 → S2 → S3		$1.16_{\pm 0.01}$	$\mathbf{1.29}_{\pm \mathbf{0.00}}$

the entire cardiac cycle [31]. CARDINAL [32] includes 239 hypertensive patients, for whom pseudo-labels were generated using a 2D+t nnU-Net for both 2CH and 4CH acquisitions and validated by an expert cardiologist.

In addition, we independently used the simulated dataset proposed by Burman *et al.* [10] described in Section II. Reference motion was extracted from the available scatterer displacements and used to derive reference temporal meshes, consistent with our simulation pipeline.

2) Evaluation: Three complementary datasets were used for evaluation. Two of them, SSHF and HUNT [33], were specifically designed for test–retest analysis and include 40 and 30 patients, respectively. For each patient, two independent recordings were acquired in the three standard apical views (A2C, A3C, and A4C), and each recording was independently analyzed by a different expert. The third dataset, HUNT-A, comprises 88 patients [34]. For each patient, a single recording was available for each of the three apical views, and each recording was independently analyzed by two experts. SSHF and HUNT enable evaluation of inter-expert agreement while accounting for probe position, cardiac-cycle selection, and tracking initialization, whereas HUNT-A evaluates inter-expert agreement without probe-position variability.

All videos were semi-automatically annotated by clinical experts using the EchoPac commercial software, which performs speckle tracking to extract myocardial points tracked over the entire cardiac cycle. The resulting annotations consist of a set of K two-dimensional points of size $T \times K \times 2$, representing the temporal tracking of the myocardial centerline. These points are subdivided into six segments for regional strain analysis. EchoPac automatically proposes to accept or reject each segment based on internal proprietary criteria, which can be manually overridden by the user. The proportions of accepted segments were 92%, 82%, and 92% for SSHF, HUNT, and HUNT-A. The myocardial centerline is represented by an average of 73 points, with a mean inter-point spacing of 2.5 mm. Reference global longitudinal strain (GLS) values were computed directly from the extracted tracking points, rather than using the GLS estimates provided by EchoPac, as the latter rely on proprietary and undisclosed computation procedures. Across all datasets, the mean peak GLS was -17.8±3.2%.

B. Track Any Speckle dataset

Our dataset, TAS-1K, comprises 1,478 synthetic echocardiographic videos, totaling 69,535 frames, along with corresponding reference myocardial motion encoded as temporal meshes. This simulated dataset was generated using the methodology described in Section III-B. The first stage relied on 242 real echocardiographic sequences drawn from the CAMUS (98 videos) and CARDINAL (144 videos) datasets. These cases were reviewed by expert clinicians to validate the accuracy of the 2D+t segmentation masks, which were obtained either through manual annotation (CAMUS) or via an automatic segmentation model (CARDINAL) [32]. This process enables the generation of the initial synthetic dataset $\mathcal{D}^0$.

The second stage relied on 1,478 real echocardiographic videos drawn from the full CAMUS (1,000 videos) and CARDINAL (478 videos) datasets. For all cases, the mesh was initialized at the ES frame, using either the manual annotations (CAMUS) or segmentations obtained from an automatic method validated by an expert clinician (CARDINAL) [32]. Inspired by the SAM framework, TAS-Net was trained on $\mathcal{D}^0$ to estimate myocardial motion for these 1,478 videos. This process enabled the generation of the $\mathcal{D}^1$ dataset and was repeated once to generate the $\mathcal{D}^2$ dataset, each comprising 1,478 synthetic videos.

Our refinement framework is flexible and supports multiple configurations, particularly with respect to the choice of simulation strategies used to model speckle decorrelation, as described in Section III-A. We therefore evaluated several configurations, summarized in Table I. For example, S1 → S1 → S1 denotes a three-stage refinement process in which the same speckle decorrelation strategy S1 is applied at all stages, whereas S1 → S2 → S3 corresponds to a progressive refinement scheme using increasingly realistic speckle decorrelation strategies across stages.

C. Model configuration

Three point-tracking models were assessed in this study.

EchoTracker. We evaluate both the EchoTracker model released with the original publication and a variant retrained on simulated data. The released model was trained on 6,490 real A2C, A3C, and A4C echocardiographic videos. Following the original training protocol, we retrained EchoTracker on simulated data. We additionally evaluated an initialization at the end-systolic (ES) frame; however, this configuration resulted in degraded performance compared with initialization at the first frame, as in the original model.

MyoTracker. MyoTracker was implemented as described in [7]. No noticeable performance difference was observed between full-resolution inputs and resized (256×256) images; therefore, the latter configuration was used. Tracking was initialized at the ES frame, which improved accuracy, as did reintroducing the iterative refinement steps.

TAS-Net. TAS-Net was built upon the CoTracker1 architecture (CoTracker1 outperformed CoTracker3 in initial tests). TAS-Net was trained with the AdamW optimizer and a one-cycle learning rate scheduler using an initial learning rate of 5×10^{-4}. Training was performed with a batch size of 1

TABLE II: Ablation study of the main contributions introduced in the design of TAS-Net. Row 1 corresponds to the baseline model described in [9]. Best values are in **bold**.

Method			SSHF - 240 videos (↓)		
Bi-window	Vis. loss	Mesh embedding	MTE (mm)	GLS MAE (%)	Folds (%)
✗	✗	✗	$1.18_{\pm 0.00}$	$1.46_{\pm 0.06}$	$27_{\pm 2}$
✓	✗	✗	$1.17_{\pm 0.00}$	$1.52_{\pm 0.01}$	$22_{\pm 1}$
✓	✓	✗	$1.16_{\pm 0.01}$	$1.42_{\pm 0.03}$	$25_{\pm 1}$
✓	✓	✓	$\mathbf{1.15}_{\pm \mathbf{0.01}}$	$\mathbf{1.32}_{\pm \mathbf{0.01}}$	$\mathbf{18}_{\pm \mathbf{1}}$

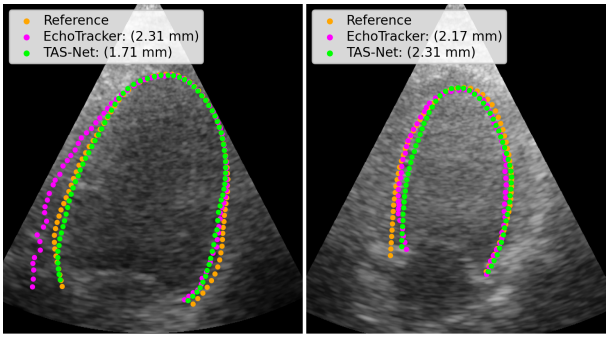

Fig. 3: Tracking results on respective worst-case sequences from the HUNT dataset for EchoTracker trained on real images [left] and TAS-Net [right], with their mean trajectory error.

and sequence lengths up to 24 frames, without padding, using full-resolution images. A sliding-window length of 8 frames was adopted, consistent with CoTracker. All experiments were initialized from publicly available pretrained checkpoints.

All models were trained for 200,000 optimization steps, and the best-performing checkpoint was selected based on the validation loss. Each model was trained on both our simulated dataset and the dataset introduced by Burman *et al.* In both cases, temporal data augmentation was applied by uniformly skipping one to three frames to emulate faster motion and variable frame rates. At inference time, EchoTracker and MyoTracker process test-set frames in 3.8 ± 0.9 ms and 3.1 ± 0.6 ms, respectively. TAS-Net processes frames in 26.7 ± 3.7 ms, which is longer but remains compatible with clinical practice. All runtimes are reported for an NVIDIA A40 GPU with 48 GB of memory. During inference, a mesh with $r = 5$ radial points is generated around the centerline for MyoTracker and TAS-Net, as these methods benefit from additional support points through joint tracking. In contrast, EchoTracker performs independent point tracking and therefore does not benefit from supplementary mesh points.

D. Evaluation

All methods were evaluated against a reference derived from the EchoPac software output, which was generated and validated by expert clinicians. Performance was assessed in terms of both geometric accuracy and application-oriented criteria by analyzing the resulting strain measurements. Only myocardial segments that were approved by expert clinicians were included in the evaluation. For all methods, we trained 3 models with different random seeds. We report mean and standard deviation values in all tables except for the strain, where one model is used, and statistical significance is reported.

1) Motion estimation metrics: We computed the mean trajectory error (MTE) between the tracked points and the corresponding reference points. We also assessed potential mesh folding by counting the number of triangle mesh cells in which the Jacobian determinant of the transformation from the initial frame ($t = 0$) to time t was negative. We report the percentage of videos with at least one fold. It is worth noting that the proportion of mesh folding is in part dependent on the mesh construction, including point spacing and radial segment orientation. While useful for assessing the spatial consistency of the estimated motion, it applies only to TAS-Net and MyoTracker, as EchoTracker only processes a myocardial centerline, and is therefore only used in our ablation study.

2) Clinical metrics: We evaluated the prediction of peak global longitudinal strain (GLS) for all methods by computing the mean absolute error (MAE) and performing a Bland–Altman analysis with respect to the reference values. In addition, a qualitative analysis of regional strain was conducted for the best-performing methods.

V. Results

A. Temporal realism of simulated ultrasound texture

We first assess the realism of each simulation strategy in terms of speckle decorrelation. This analysis was conducted on the 98 patients from CAMUS with available ground-truth segmentations. Each sequence was simulated using the three strategies described in Section III-A, without any refinement stage. Pointwise correlations between the reference ES frame and each subsequent frame were computed at every mesh location. These correlations were then compared with the corresponding values computed from the real sequences. Quantitative comparisons were performed using the mean absolute error (MAE). The S1, S2 and S3 strategies had MAEs of 0.149 ± 0.051, 0.119 ± 0.029 and 0.077 ± 0.013 respectively.

The results indicate that strategies S2 and S3 substantially improve speckle decorrelation modeling compared with S1, with S3 yielding the closest match to real data. Qualitative results are illustrated in Figure 2 for the three proposed strategies as well as for the dataset of Burman *et al.* Since the latter is derived from a different subset of CAMUS patients, a strict quantitative comparison is not possible. The figure displays the correlation curves for the 36 myocardial centerline points and illustrates the increased diversity and closer agreement of speckle decorrelation patterns obtained with strategies S2 and S3 compared with the real data.

B. Effectiveness of the multi-stage simulation strategy

Table I reports the performance of TAS-Net on SSHF and HUNT for different configurations of the refinement strategy, considering both the number of refinement stages and the simulation strategies used to model speckle decorrelation. First, we observe that performance generally improves with the number of refinement stages, particularly on HUNT. However, using simulation strategy S2 without refinement leads to

TABLE III: Mean trajectory error (MTE, mm) across datasets and views for the evaluated methods. Best scores are indicated in **bold** for methods trained on synthetic data.

Method	Dataset	SSHF - 240 videos (↓)			HUNT - 180 videos (↓)			HUNT-A - 588 videos (↓)		
		A2C	A3C	A4C	A2C	A3C	A4C	A2C	A3C	A4C
EchoTracker	Real	1.21	1.09	1.10	1.45	1.32	1.27	1.26	1.15	1.04
EchoTracker	Burman	2.30±0.05	2.18±0.04	2.26±0.05	3.28±0.05	2.64±0.01	2.99±0.05	3.41±0.04	2.63±0.02	2.86±0.03
MyoTracker	Burman	2.42±0.06	2.59±0.09	2.56±0.06	3.35±0.14	2.70±0.07	2.99±0.08	3.26±0.06	2.77±0.08	3.03±0.09
TAS-Net	Burman	1.71±0.08	1.54±0.07	1.49±0.07	2.54±0.05	1.96±0.10	2.08±0.10	2.33±0.09	1.90±0.15	1.95±0.11
EchoTracker	TAS-1K	1.57±0.04	1.56±0.07	1.49±0.02	2.07±0.05	2.02±0.07	1.79±0.05	1.93±0.04	1.98±0.04	1.68±0.03
MyoTracker	TAS-1K	1.49±0.01	1.49±0.03	1.43±0.06	1.80±0.05	1.79±0.08	1.49±0.05	1.68±0.05	1.71±0.05	1.40±0.05
TAS-Net	TAS-1K	**1.22±0.00**	**1.12±0.00**	**1.12±0.01**	**1.42±0.01**	**1.19±0.00**	**1.21±0.01**	**1.33±0.00**	**1.17±0.01**	**1.07±0.00**

inferior performance, which can be attributed to overfitting when training on a small dataset (242 samples). Similarly, S2 → S2 underperforms compared with S1 → S1. This can be explained by the fact that suboptimal motion estimates obtained at the first stage propagate to subsequent stages, limiting overall performance. Based on these observations, we propose a multi-stage strategy in which the realism of speckle decorrelation is progressively increased across stages, resulting in increasingly challenging training datasets. This motivates the S1 → S2 → S3 configuration, which achieves the best overall performance across SSHF and HUNT. Based on these observations, we retain this best-performing configuration for the remaining experiments. The corresponding simulated dataset is hereafter referred to as TAS-1K.

C. Ablation study of the proposed TAS-Net model

An ablation study using SSHF evaluates the individual contributions introduced in TAS-Net to improve upon the CoTracker framework for point tracking. Results are reported in Table II. Performance was evaluated both in terms of geometric (MTE, folds) and clinical (GLS) metrics. Improved performance in terms of MTE is observed across all proposed contributions. Both the continuous visibility loss and the mesh embedding lead to improved GLS and MAE. Notably, the mesh embedding is the only contribution that substantially reduces mesh folding, highlighting the importance of enabling TAS-Net to explicitly distinguish points based on their mesh indices. In comparison, MyoTracker, trained on the same data, produces mesh folding in $63 \pm 6\%$ of SSHF videos.

D. Comparisons with state-of-the-art methods

TAS-Net was compared with Echotracker and MyoTracker. These methods were trained on both the simulated dataset proposed by Burman et al. and our proposed TAS-1K dataset.

Motion estimation scores. Table III displays the MTE scores obtained by each method on SSHF, HUNT and HUNT-A on the A2C, A3C and A4C cardiac views. For all evaluated methods, training on the TAS-1K synthetic dataset leads to the best performance across the validation datasets and views, indicating the effectiveness of the proposed simulation strategy. Also, TAS-Net outperformed MyoTracker and EchoTracker, regardless of the synthetic dataset used for training. These results support the effectiveness of the proposed architectural choices, in particular the use of a CoTracker-based architecture leveraging pre-trained weights on a large-scale dataset.

Finally, we compared TAS-Net trained on the TAS-1K synthetic dataset with EchoTracker trained on real echocardiographic videos, using myocardial motion references extracted from EchoPac. Although this comparison is inherently biased, as both EchoTracker's training dataset and our validation dataset (two distinct datasets) use EchoPac-derived annotations, the two methods show comparable performance. This suggests that the proposed approach can be competitive when trained exclusively on synthetic data. Figure 3 presents a qualitative comparison of TAS-Net and EchoTracker, trained on real data, focusing on the worst-performing samples in terms of MTE. It shows that EchoTracker exhibits severe tracking errors, whereas TAS-Net remains closer to the EchoPac reference, with discrepancies that are more limited in magnitude.

Global longitudinal strain scores. Table IV reports the performance of the different methods for peak GLS estimation on the test–retest datasets (combining SSHF and HUNT) and on the agreement dataset (HUNT-A). Consistent with the geometric metrics, training on the TAS-1K synthetic dataset yields the best results. Again, TAS-Net outperformed both MyoTracker and EchoTracker. Our model also produced comparable results compared to EchoTracker trained on real data with the reference motion extracted from EchoPac. Notably, the performance of TAS-Net is on par with the inter-observer variability measured in both the test–retest and agreement settings, suggesting good robustness under clinical acquisition conditions. This observation is further supported by the Bland–Altman plots shown in the first column of Figure 4, computed on the agreement dataset. These plots indicate a near-zero bias and limits of agreement below 5% between GLS estimates obtained with TAS-Net and clinician references.

Both the MAE metric and Bland–Altman analysis show an increased variability between the test-retest setting and the agreement setting, showing the impact of the added variability induced by the probe position. However, in both cases TAS-Net exhibits a level of robustness to all forms of variability on par with the reference obtained with EchoPac.

E. Regional Strain

We investigate the ability of TAS-Net to estimate regional longitudinal strain (RLS) from echocardiographic videos. The Bland–Altman plots given in Figure 4 compare RLS estimates

TABLE IV: Peak GLS estimation performance, mean absolute error (MAE) and Bland–Altman statistics (μ and σ), with respect to the reference and in a test–retest/agreement setting. For methods trained on synthetic data, best values are indicated in **bold** and * indicates statistically significant difference from all other methods for the MAE metric (paired one-tailed t-test, $p \leq 0.05$).

Method	Dataset	SSHF+HUNT (↓)						HUNT-A (↓)					
		Reference - 420 videos			Test-retest - 210 videos			Reference - 588 videos			Agreement - 264 videos		
		MAE	μ	σ	MAE	μ	σ	MAE	μ	σ	MAE	μ	σ
Reference		-	-	-	2.02	-0.10	2.77	-	-	-	1.78	0.78	2.15
EchoTracker	Real	1.59	0.59	1.94	1.98	-0.03	2.57	1.50	0.95	1.85	1.14	0.34	1.47
EchoTracker	TAS-1K	3.52	3.37	2.61	2.69	**0.06**	3.57	3.85	3.67	3.09	1.97	**-0.15**	2.64
MyoTracker	TAS-1K	2.12	1.67	2.17	2.62	0.23	3.39	2.31	1.96	2.47	1.65	0.43	2.21
TAS-Net	TAS-1K	**1.52***	**1.02**	**1.64**	**2.04***	0.28	**2.71**	**1.39***	**0.91**	**1.61**	**1.42***	0.33	**1.86**

obtained with the proposed model and with two expert clinicians on HUNT-A. RLS was computed for the 18 segments (6 per view) following the AHA definition We perform the analysis on HUNT-A, which measures the agreement of two experts using EchoPac on the same video acquisition. For each segment, three comparisons are considered: (i) TAS-Net vs. reference, where each reference is considered independently, and TAS-Net is initialized with the reference centerline at ES (T vs. R); (ii) a TAS-Net agreement measuring configuration, where we compare the TAS-Net prediction with the different initialization performed by each expert (T vs. T), and (iii) an expert agreement analysis, where two independent experts' references, obtained with EchoPac, are compared (R vs. R).

An analysis of inter-expert variability across all three views reveals limits of agreement below 10% for mid-inferior segments, ∼10% for basal and mid-anterior segments, and slightly above 10% for apical segments, confirming the lower reproducibility of RLS compared to GLS. Across all segments, the variability observed between TAS-Net and Expert 1, as well as the test–retest variability of TAS-Net, is of the same order of magnitude as the inter-expert variability. A qualitative example of RLS prediction is given in Figure 5. These results indicate that the proposed approach can achieve reproducible performance comparable to that of expert clinicians, despite being trained exclusively on synthetic data.

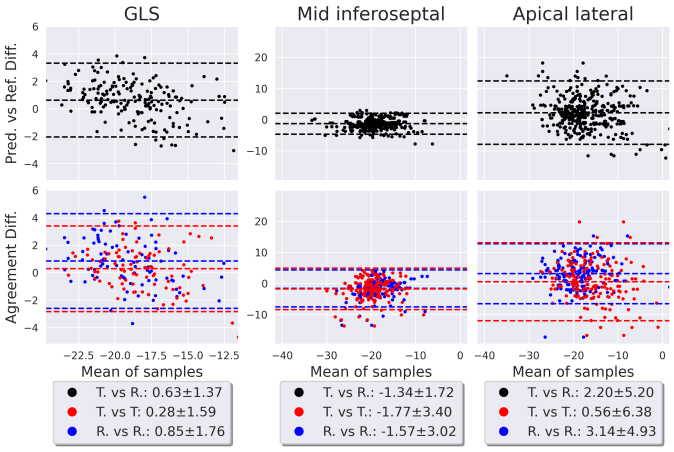

Fig. 4: Bland–Altman analysis of TAS-Net (T) for GLS and RLS (best and worst segments), evaluated against measurements from an expert using EchoPac (T vs. R) and in an inter-expert agreement evaluation setting (T vs. T and R vs. R) on the A4C sequences of the HUNT-A dataset.

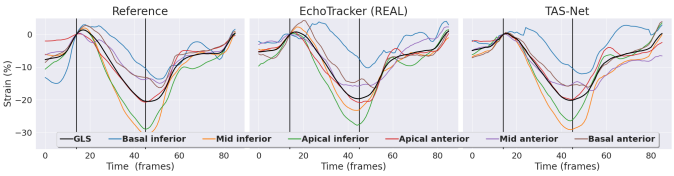

Fig. 5: Regional strain curves from the best-performing deep learning methods [middle and right] compared with those from a clinical expert using EchoPac [left].

VI. Discussions and Conclusions

Feasibility of synthetic-only training. In this study, we show that the proposed strategies to enhance the realism of synthetic datasets, in terms of both speckle decorrelation and myocardial motion, enable training deep learning models with improved performance compared to existing synthetic datasets. In particular, the proposed multi-stage refinement strategy, incorporating progressively increasing levels of speckle realism, consistently outperformed the other evaluated configurations. We also demonstrate that designing a dedicated point-tracking model based on the CoTracker architecture, leveraging large-scale pre-trained weights and adapting it to the characteristics of echocardiographic videos, is key to achieve highly competitive performance. Comparisons on the test–retest and agreement datasets show that TAS-Net achieves performance comparable to inter-expert variability for both motion and peak GLS estimation. To the best of our knowledge, such a level of agreement between a synthetic-only trained model and expert variability has not been previously reported. Our approach therefore has strong potential to improve the robustness of peak GLS measurements under clinical acquisition conditions.

Generalization across dataset, views and pathologies. A key contribution of this work is to demonstrate that the generation of realistic synthetic datasets enables the generalization of deep learning models to real echocardiographic videos. This generalization ability was further evaluated across views. While TAS-1K only includes synthetic videos from the A4C and A2C views, the validation datasets comprise all three stan-

dard views (A4C, A2C, A3C). As shown in Table III, TAS-Net achieves comparable performance across views, indicating consistent behavior despite the absence of A3C data during training. Also, TAS-Net attains performance comparable to EchoTracker, which is trained on real data incorporating all three views. This underlines that our approach generalizes well across both datasets and echocardiographic views and diseases. Finally, TAS-Net's GLS error with respect to the EchoPac reference varies by at most 0.6% across all disease categories in the evaluation dataset (hyperlipidemia, hypertension, diabetes, angina, and coronary artery disease), suggesting good generalization across different clinical conditions.

Deep learning methods for regional strain estimation. The inter-expert variability shown in Figure 4 highlights the limited reproducibility of regional strain across experts. While some segments (e.g. mid-inferior) exhibit variability comparable to that observed for GLS, most segments present limits of agreement around 10%, which remains high for routine clinical use. TAS-Net achieves a level of accuracy and reproducibility comparable to clinical inter-expert variability. However, these results are influenced by the use of manual expert annotations at ES to initialize the tracking procedure. This initialization step inherently introduces human variability, both in the selection of the ES frame and in the delineation of the myocardial contour. As a result, the reported performance of TAS-Net incorporates this source of variability. This limitation could be mitigated by replacing manual initialization with an automatic segmentation approach for both ES frame selection and initial contour placement. This extension is beyond the scope of this study, but it will be investigated in future work.

Limitations and future work. EchoPac outputs do not provide a direct measurement of true myocardial motion. This is partially mitigated by restricting the evaluation to myocardial segments validated by clinicians and by assessing performance on both test–retest and agreement datasets. Nevertheless, future work should include validation against independent reference modalities, such as cardiac MR or tagged MR imaging, to enable a more objective assessment of strain accuracy.

REFERENCES

[1] R. M. Lang *et al.*, "Recommendations for cardiac chamber quantification by echocardiography in adults," *Eur Heart J Cardiovasc Imaging*, vol. 16, pp. 233–71, 2015.

[2] M. Cikes and S. D. Solomon, "Beyond ejection fraction: An integrative approach for assessment of cardiac structure and function in heart failure," *Eur Heart J*, vol. 37, pp. 1642–50, 2016.

[3] S. Olaisen *et al.*, "Automatic measurements of left ventricular volumes and ejection fraction by artificial intelligence: clinical validation in real time and large databases," *Eur Heart J Cardiovasc Imaging*, vol. 25, pp. 383–95, 2023.

[4] O. A. Smiseth, O. Rider, M. Cvijic, L. Valkovič, E. W. Remme, and J.-U. Voigt, "Myocardial Strain Imaging," *JACC Cardiovasc Imaging*, vol. 18, pp. 340–81, 2025.

[5] C. G. Mihos *et al.*, "Speckle-Tracking Strain Echocardiography for the Assessment of Left Ventricular Structure and Function," *Circulation*, vol. 152, 2025.

[6] M. A. Azad *et al.*, "EchoTracker: Advancing Myocardial Point Tracking in Echocardiography," in *MICCAI 2024*, 2024, vol. 15004, pp. 645–55.

[7] A. Chernyshov *et al.*, "Low Complexity Point Tracking of the Myocardium in 2D echocardiography," *arXiv:2503.10431*, 2025.

[8] E. Evain *et al.*, "Motion estimation by deep learning in 2D echocardiography: Synthetic dataset and validation," *IEEE TMI*, vol. 41, pp. 1911–24, 2022.

[9] A. A. Taskén *et al.*, "Estimation of Segmental Longitudinal Strain in Transesophageal Echocardiography by Deep Learning," *IEEE JBHI*, vol. 30, pp. 436–47, 2026.

[10] N. Burman, C. A. Manetti, S. V. Heymans, M. Ingram, J. Lumens, and J. D'hooge, "Large-scale simulation of realistic cardiac ultrasound data with clinical appearance: Methodology and open-access database," *IEEE Access*, vol. 12, pp. 117 040–55, 2024.

[11] N. Karaev, I. Rocco, B. Graham, N. Neverova, A. Vedaldi, and C. Rupprecht, "CoTracker: It Is Better to Track Together," in *ECCV*, 2025, vol. 15120, pp. 18–35.

[12] D. Sun, X. Yang, M.-Y. Liu, and J. Kautz, "Pwc-net: Cnns for optical flow using pyramid, warping, and cost volume," in *CVPR*, 2018, pp. 8934–43.

[13] Z. Teed and J. Deng, "RAFT: Recurrent All-Pairs Field Transforms for Optical Flow," in *ECCV*, 2020, pp. 402–19.

[14] C. Doersch *et al.*, "Tap-vid: A benchmark for tracking any point in a video," *NeurIPS*, vol. 35, pp. 13 610–26, 2022.

[15] K. Greff *et al.*, "Kubric: A scalable dataset generator," in *CVPR*, 2022, pp. 3749–61.

[16] Y. Zheng, A. W. Harley, B. Shen, G. Wetzstein, and L. J. Guibas, "Pointodyssey: A large-scale synthetic dataset for long-term point tracking," in *ICCV*, 2023, pp. 19 855–65.

[17] A. W. Harley, Z. Fang, and K. Fragkiadaki, "Particle Video Revisited: Tracking Through Occlusions Using Point Trajectories," in *ECCV*, 2022, vol. 13682, pp. 59–75.

[18] C. Doersch *et al.*, "Tapir: Tracking any point with per-frame initialization and temporal refinement," in *ICCV*, 2023, pp. 10 061–72.

[19] N. Karaev, Y. Makarov, J. Wang, N. Neverova, A. Vedaldi, and C. Rupprecht, "Cotracker3: Simpler and better point tracking by pseudo-labelling real videos," in *ICCV*, 2025, pp. 6013–22.

[20] D. Garcia, P. Lantelme, and E. Saloux, "Introduction to speckle tracking in cardiac ultrasound imaging," *Speckle filtering and tracking in cardiovascular ultrasound imaging and video*, pp. 571–98, 2018.

[21] S. Ünlü *et al.*, "Inter-vendor variability in strain measurements depends on software rather than image characteristics," *Int J Cardiovasc Imaging*, vol. 37, 2021.

[22] D. Garcia, "SIMUS: An open-source simulator for medical ultrasound imaging. Part I: Theory & examples," *Comput Methods Programs Biomed*, vol. 218, p. 106726, 2022.

[23] T. Arts, T. Delhaas, P. Bovendeerd, X. Verbeek, and F. W. Prinzen, "Adaptation to mechanical load determines shape and properties of heart and circulation: The CircAdapt model," *Am J Physiol Heart Circ Physiol*, vol. 288, pp. 1943–54, 2005.

[24] H. Gao *et al.*, "A fast convolution-based methodology to simulate 2-Dd/3-D cardiac ultrasound images," *IEEE TUFFC (56)*, pp. 404–9, 2009.

[25] B. Brady, G. King, R. Murphy, and D. Walsh, "Myocardial strain: a clinical review." *Inter J Med Sci*, vol. 16, pp. 1–8, 2022.

[26] V. Perrot, M. Polichetti, F. Varray, and D. Garcia, "So you think you can das? a viewpoint on delay-and-sum beamforming," *Ultrasonics*, vol. 111, p. 106309, 2021.

[27] M. Alessandrini *et al.*, "Realistic vendor-specific synthetic ultrasound data for quality assurance of 2-d speckle tracking echocardiography: Simulation pipeline and open access database," *IEEE TUFFC*, vol. 65, pp. 411–22, 2018.

[28] A. Kirillov *et al.*, "Segment anything," in *ICCV*, 2023, pp. 4015–26.

[29] A. Judge *et al.*, " Domain Adaptation of Echocardiography Segmentation Via Reinforcement Learning ," in *MICCAI*, 2024.

[30] S. Leclerc *et al.*, "Deep learning for segmentation using an open large-scale dataset in 2D echocardiography," *IEEE TMI*, pp. 2198–210, 2019 (38).

[31] N. Painchaud, N. Duchateau, O. Bernard, and P.-M. Jodoin, "Echocardiography segmentation with enforced temporal consistency," *IEEE TMI*, vol. 41, pp. 2867–78, 2022.

[32] H. J. Ling, N. Painchaud, P.-Y. Courand, P.-M. Jodoin, D. Garcia, and O. Bernard, "Extraction of Volumetric Indices from Echocardiography: Which Deep Learning Solution for Clinical Use?" in *FIMH*, 2023, vol. 13958, pp. 245–54.

[33] I. M. Salte *et al.*, "Deep learning for improved precision and reproducibility of left ventricular strain in echocardiography: A test-retest study," *Journal of the American Society of Echocardiography*, vol. 36, no. 7, pp. 788–799, 2023, 34th ASE Annual Scientific Sessions.

[34] J. Nyberg *et al.*, "Echocardiographic reference ranges of global longitudinal strain for all cardiac chambers using guideline-directed dedicated views," *JACC: Cardiovascular Imaging*, vol. 16, no. 12, pp. 1516–1531, 2023.